Dalton Transactions

ROYAL SOCIETY OF CHEMISTRY

PAPER

View Article Online
View Journal | View Issue

Cite this: *Dalton Trans.*, 2025, **54**, 11246

$ZnIn_2S_4$ combined with a flower-like NiAl-layered double hydroxide with enhanced photocatalytic H_2 production activity†

Anna P. Souri,[a,b] Onur Cavdar,[b] Maria Zografaki,[a,c] Leila Zouridi,[a,d] Vassilios Binas,[a,c] Tomasz Klimczuk,[e,f] Kostiantyn Nikiforow[g] and Anna Malankowska *[b]

A novel $ZnIn_2S_4$/NiAl-layered double hydroxide (LDH)/Pt heterojunction was developed as a highly efficient photocatalyst for photocatalytic hydrogen evolution (PHE) under UV-vis and visible (λ > 420 nm) irradiation. ZIS was decorated with NiAl-LDH microflowers using an oil bath at 80 °C, followed by modification through Pt photodeposition. Our results demonstrated that using an *in situ* growth method for decorating ZIS with NiAl-LDH considerably enhanced PHE reactions. The effect of Pt photodeposition on the $ZnIn_2S_4$/NiAl-LDH heterojunction composites in photocatalytic hydrogen generation under irradiation was also studied. The introduction of an optimal amount of 0.17 wt% Pt on the surface of ZIS/NiAl25 increased the H_2 production rate by approximately 6.5 times compared with bare ZIS under visible light irradiation. Hydrogen production was elevated from 171 to 1665 μmol g^{-1} h^{-1} under UV-vis light for ZIS and ZIS/NiAl/1.95Pt, representing a 9.6-fold increase. Additionally, a proposed mechanism for PHE over the $ZnIn_2S_4$/NiAl-LDH/Pt heterojunction was explored. This work contributes to the development of advanced nanoscale materials for energy sustainability, demonstrating their role in addressing global energy challenges through clean and efficient hydrogen evolution processes under visible and UV-vis light irradiation.

Received 30th April 2025,
Accepted 30th June 2025

DOI: 10.1039/d5dt01018g

rsc.li/dalton

1. Introduction

The depletion of fossil fuels and their impact on the environment and our health have made the quest for renewable and sustainable energy sources critically important. As a result, semiconducting materials for water splitting are regarded as suitable candidates in addressing this global issue, given that H_2 is a green fuel and abundant in nature. Among the various semiconducting materials studied for photocatalytic water splitting, layered double hydroxides and sulfides have gained attention owing to their promising properties and versatility.[1,2] Layered double hydroxide (LDH) catalysts have been widely employed and studied for various applications such as electrocatalysis,[3] photocatalytic H_2 production,[4] pollutant degradation,[5] and CO_2 conversion.[6] The extensive research attention they have garnered stems from their unique layered structure, compositional flexibility, and the variety of structures they can form, as well as their chemical and thermal stability. LDHs exhibit a lamellar structure consisting of brucite-like layers of divalent and trivalent cations, with the chemical formula $[M^{2+}_{1-x}M^{3+}_{x}]^{x+}(A^{n-})_{x/n}{\cdot}mH_2O$, where M represents the divalent or trivalent cation (usually a transition metal), A is the interstitial anion between the layers, n is the charge of the interlayer species, and m is the number of water molecules. More specifically, positively charged brucite-type octahedral sheets alternate with interlayers containing carbonate anions. The compositional versatility of this material family, combined with different synthetic routes, is the reason for reporting several morphologies.[7] These materials can form various shapes including 2D structures like hexagonal plates[8] and 3D structures resembling flower-like shapes,[9] which in turn influence

[a]*Institute of Electronic Structure and Laser, Foundation for Research and Technology-Hellas, 71110 Heraklion, Greece*
[b]*Department of Environmental Technology, Faculty of Chemistry, University of Gdansk, 80-308 Gdansk, Poland. E-mail: anna.malankowska@ug.edu.pl*
[c]*Department of Chemistry, Aristotle University of Thessaloniki, Thessaloniki, Greece*
[d]*Department of Materials Science and Technology, University of Crete, Heraklion, Greece*
[e]*Faculty of Applied Physics and Mathematics, Gdansk University of Technology, Narutowicza, Gdansk, Poland*
[f]*Advanced Materials Center, Gdansk University of Technology, Narutowicza, Gdansk, Poland*
[g]*Institute of Physical Chemistry, Polish Academy of Sciences, Kasprzaka 44/52, 01-224 Warsaw, Poland*
† Electronic supplementary information (ESI) available. See DOI: https://doi.org/10.1039/d5dt01018g

their properties. Nevertheless, LDHs suffer from low electrical conductivity and insufficient effective sites, which negatively affect their catalytic abilities. Recent studies have shown that tailoring the interlayer composition and thickness of LDHs can significantly improve their electrocatalytic performance. Jiang *et al.* synthesized ultrathin sulfate-intercalated NiFe-LDH nanosheets *via* a solvothermal method, achieving a high oxygen evolution reaction (OER) activity with a low overpotential (212 mV at 10 mA cm^{-2}) and excellent durability over 11 hours.[10] The enhanced activity was attributed to the ultrathin morphology, increased interlayer spacing due to SO_4^{2-} anions, and uniform nanosheet structure, all of which facilitated charge transfer and active site accessibility.[10] Zhao *et al.* demonstrated that introducing multiple structural defects—namely, holey morphology, oxygen vacancies, and Ni^{3+} species—into NiFe-LDH nanosheets *via* a green H_2O_2-assisted etching method significantly enhanced their oxygen evolution reaction (OER) performance, achieving an overpotential as low as 170 mV at 10 mA cm^{-2}.[11] Zhao *et al.* demonstrated that dual Fe^{3+}/BF_4^- doping in NiFe-MOF nanosheets significantly boosts OER performance through electronic structure tuning and improved surface reactivity—an approach conceptually relevant to LDH modification strategies.[12]

Metal sulfides, by contrast, are a category that has been meticulously studied owing to their status as primarily narrow band gap semiconductors, which allows them to be activated under visible irradiation.[13,14] The ternary compound $ZnIn_2S_4$ (ZIS) serves as an excellent example, as its band positions are suitable for various photocatalytic redox reactions. Additionally, it exhibits improved chemical stability compared with other metal sulfides and is low cost.[2] Of the two major crystal structures, hexagonal and cubic phases, the hexagonal phase is more commonly employed because of its higher photocatalytic activity.

In the literature, efforts to combine the advantages of ZIS and LDHs by pairing them have been reported, primarily for hydrogen evolution reactions and Cr(VI) reduction (Table S1†). More specifically, Deng *et al.*[15] paired ZIS with LDH NiAl, featuring flower-like structures, and added carbon quantum dots (C QDs) as a co-catalyst. The composite with the optimal carbon dot concentration exhibited a rate of 23.1 mmol g^{-1} h^{-1} under visible light, which was 16.4 and 1.4 times higher than ZIS and ZIS/NiAl, respectively. Additionally, Zhao *et al.*[16] formed *in situ* ZIS on MIL-88A-derived Ni–Fe LDH, creating ternary-shelled nanotubes for photocatalytic hydrogen production. Their optimal heterostructure achieved a rate of 2.0 mmol g^{-1} h^{-1} under visible light irradiation. Yang *et al.*[17] decorated hexagonal sheets of MgAl LDH with ZIS through a water bath heating method and tested its effectiveness in Cr(VI) reduction and H_2 evolution. Their optimal sample reached a rate of 1.9 mmol g^{-1} h^{-1} under visible light. Ma *et al.* reported a $Zn_{0.2}Cd_{0.8}S/Zn_{0.2}Cd_{0.8}$-MOF heterostructure with well-aligned energy bands and strong interfacial interactions, which facilitated efficient charge separation and significantly improved hydrogen evolution efficiency.[18] Furthermore, the group led by He[19] paired CoAl with ZIS by *in situ* growth of the latter on the LDH to form a 2D/2D S-scheme heterostructure. The optimal mass ratio of LDH/ZIS was 1 : 2, resulting in an H_2 production rate of 1.5 mmol g^{-1} h^{-1} under simulated sunlight. A similar combination was carried out by Peng *et al.*[20] in a study where transition metal chalcogenides $CdIn_2S_4$, In_2S_3, and $ZnIn_2S_4$ were combined with CoAl LDH for H_2 production. Their optimal ZIS/CoAl photocatalyst exhibited an H_2 rate of 1.2 mmol g^{-1} h^{-1} under visible light. Tang *et al.*[21] prepared a NiCoFe-LDH@ZIS Z-scheme heterojunction for simultaneous H_2 evolution with benzylamine oxidation, achieving a H_2 rate of 113.57 mmol g^{-1} h^{-1} and a 97.78% conversion rate of benzylamine oxidation. Other groups, however, such as that of Wang,[22] combined ZIS nanosheets with leaf-like NiCo LDH to create a core–shell composite for Cr(VI) reduction under visible irradiation, whereas Zho[23] synthesized a 1D/2D CoNi-LDH/$ZnIn_2S_4$ S-scheme heterojunction for tetracycline degradation under a photocatalytic-peroxymonosulfate activation system.

Herein, inspired by the aforementioned literature, we present for the first time the pairing of ZIS nanosheets with a 3D flower-like NiAl-LDH to form a composite heterostructure with Pt as a co-catalyst for photocatalytic hydrogen evolution (PHE). The ZIS/NiAl composite was synthesized through an *in situ* growth method, and the addition of the Pt co-catalyst was achieved *via* photochemical reduction. The Pt photodeposited composites (ZIS/NiAl/Pt) were tested under UV-vis and visible irradiation to study the effects of the metal under different irradiation conditions. Additionally, experiments comparing the rate of our optimal catalysts in UV-vis with that of commercial P25 were conducted. Finally, by incorporating X-ray photoelectron spectroscopy (XPS) analysis, electrochemical impedance spectroscopy, and DRS data, insights into the mechanism of the system were obtained, providing a possible explanation for the outstanding stability of the ZIS/NiAl heterostructure. To the best of our knowledge, the combination of metal nanoparticles with the ZIS/LDH heterostructure and the meticulous study of UV-vis and visible irradiation has not been reported in any other publication. This research offers valuable insights into environmentally relevant nanomaterial interactions, emphasizing the development of photoactive and stable materials under safe and sustainable design principles.

2. Experimental section

2.1 Synthesis of NiAl-LDH

For the preparation of NiAl-LDH, 558 mg of $Ni(NO_3)_2{\cdot}6H_2O$, 200 mg of $Al(NO_3)_3{\cdot}9H_2O$, 190 mg of NH_4F, and 768 mg of urea were dissolved in 80 mL of deionized water (DI), followed by 30 minutes of sonication treatment. The resulting green solution was then transferred to a Teflon autoclave and heated at 120 °C for 24 hours. Once the autoclave had cooled to 24 °C, the solution was centrifuged and washed twice with deionized water and three times with ethanol. Finally, the sample was dried in an oven at 70 °C overnight.[24] The obtained sample is denoted as NiAl (Fig. 1a).

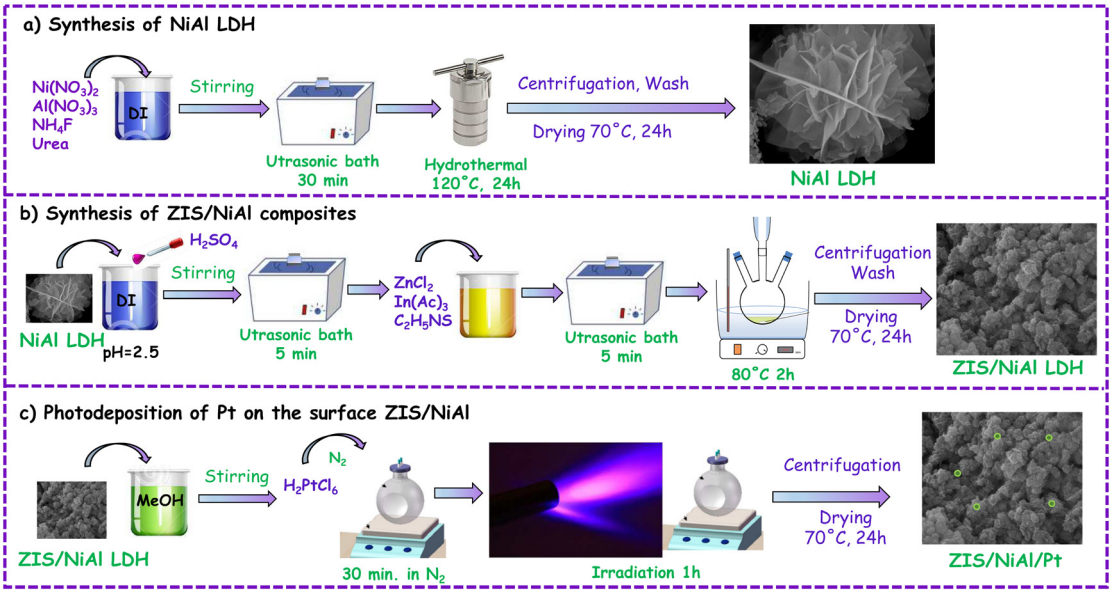

Fig. 1 Schematic of the synthesis of (a) NiAl-LDH; (b) ZIS/NiAl-LDH composite; (c) ZIS/NiAl/Pt composite.

2.2. Synthesis of ZIS and ZIS/NiAl heterostructures

Various amounts of preprepared NiAl (12.5, 25, and 50 mg) were dispersed in 60 mL of deionized (DI) water, with the pH adjusted to 2.5 using 0.1 M H_2SO_4, and sonicated for 5 minutes. Subsequently, 272 mg of $ZnCl_2$, 602 mg of $In(Ac)_3$, and 300 mg of thioacetamide were added to the solution, which was sonicated again for 5 minutes. The mixture was then transferred to a 100 mL three-necked round-bottom flask, equipped with a condenser, and placed in an oil bath, where it was heated to 80 °C for 2 hours under magnetic stirring. The resulting products were purified using water and isopropanol through centrifugation and dried at 70 °C overnight.[25] The obtained samples are designated as ZIS/NiAlx, where x = 12, 25, and 50. For pristine ZIS, the same synthetic route was followed without the addition of NiAl, and the resulting sample is denoted as ZIS (Fig. 1b).

2.3. Photodeposition of Pt nanoparticles

The Pt-loaded ZIS/NiAl composites were synthesized through a photochemical reduction method. In a typical procedure, 100 mg of ZIS/NiAl25 catalyst was dissolved in an aqueous solution (10 mL) containing 20% (v/v) methanol under vigorous stirring. A nominal amount of $H_2PtCl_6{\cdot}6H_2O$, dissolved in water (C = 0.05 M), was then added to the suspension while stirring, and the resulting mixture was purged with N_2 for 30 minutes. The solution was subsequently irradiated for 1 hour under continuous stirring with a 1000 Watt Xe lamp. The temperature was maintained at 10 °C during the irradiation. Centrifugation followed, along with three washes with water and one wash with ethanol, after which the samples were dried at 70 °C. The samples are denoted as ZIS/NiAl25/yPt, where y = 0.17, 0.66, 1.3, 1.95, and 2.6 indicates the wt% of the metal. For the case of P25 loaded with Pt, the same procedure was followed, and the sample is denoted as P25/1.95Pt. The calculations for the appropriate wt% are included in the ESI† (Fig. 1c).

2.4. Physical characterization

Surface morphology and elemental analysis of the samples were conducted using Scanning Electron Microscopy (SEM) using a JEOL JSM-6390LV instrument at an accelerating voltage of 20 kV, equipped with an Oxford INCA PentaFETx3 Energy Dispersive X-ray Spectroscopy (EDX) detector (Oxfordshire, UK), and a FE-SEM (Jeol 7000) operating at 15 keV. The morphological features of the materials were also examined using Transmission Electron Microscopy (TEM) at an accelerating voltage of 200 kV (JEOL-2100 instrument equipped with a LaB_6 filament).

X-ray powder diffraction (XRD) analysis was conducted using a Bruker diffractometer equipped with a CuKα radiation source (λ = 1.5404 Å). Raman measurements were performed at room temperature using a XYZ Raman spectrometer with a 532 nm laser as the excitation source. The laser power was set to 5 mW to prevent destructive interaction with the samples owing to the presence of sulfide and hydroxide ligands. The laser beam was focused on each sample through a confocal microscope with a 50× objective. Measurements were acquired with an exposure time of 10 Hz, comprising five consecutive scans at low resolution (±2 cm^{-1}). The specific measurement location for each sample was recorded as an image using the confocal microscope.

Fourier-transform infrared spectroscopy (FTIR) (Thermo Scientific, Nicolet iS5) was used to identify the surface characteristics of prepared samples in the scan range of 500–4000 cm^{-1} in the diffuse reflectance mode at room temperature, with KBr serving as the reference material. To analyze

the emission of light following excitation, photoluminescence (PL) measurements were conducted at room temperature using an LS-50B luminescence spectrophotometer. This instrument was equipped with a Xenon (Xe) discharge lamp as the excitation source and an R928 photomultiplier as the detector. The samples were excited at 330 nm, and the emission was scanned between 300 and 800 nm.

DRS spectra for powders were acquired using a UV-vis spectrophotometer (UV 2600, Shimadzu) equipped with four integrating spheres, covering the wavelength range of 300–800 nm. XPS measurements were conducted using a PHI VersaProbe 5000 scanning spectrometer (ULVAC-PHI; Chigasaki, Japan). The XPS spectra were recorded using monochromatic Al-Kα radiation ($h\nu$ = 1486.6 eV) from an X-ray source operating at a 100 μm spot size, 25 W, and 15 kV. High-resolution (HR) XPS spectra were collected with an analyzer pass energy of 23.5 eV and an energy step size of 0.1 eV. Casa XPS software (v.2.3.25, Casa Software Ltd, Wilmslow, United Kingdom) was used to analyze the XPS data. For quantification, the PHI sensitivity factors and the determined transmission function of the spectrometer were employed.

2.5. Photocatalytic H_2 production experiments

In total, 25 mg of catalyst were dissolved in 20 mL of a triethanolamine (TEOA) solution (10% (v/v)). The solution was sonicated for 2 minutes to ensure proper dispersion of the powder, then transferred to the reactor, sealed with a plastic septum, and purged with N_2 for 30 minutes in the dark. After purging, the solution was irradiated by a 1000 Watt Xe lamp for 4 hours. The reactor was connected to a water cooling system that maintained a steady temperature of 10 °C. The evolved H_2 gas was monitored every hour by collecting 200 μL of gas using an air-tight syringe (Hamilton) from the headspace of the reactor and analyzing it in a gas chromatograph (GC, Thermo Scientific TRACE 1300-GC, N_2 carrier). No hydrogen was evolved in the absence of the photocatalyst under the same conditions.

2.6. Action spectra analysis for photocatalytic hydrogen evolution reaction

Hydrogen evolution over the most active sample for the quantum efficiency experiments was initiated in a cell (QS High Precision Cell, Hellma Analytics) which is made of a high performance quartz glass with a screw top with hole sealed with a silicone rubber septum (light path: 10 mm, thickness of the quartz glass: 1 mm) filled with 3 ml of photocatalytic hydrogen evolution mixture with the same concentration of the photocatalyst powder and sacrificial reagent as in the photocatalytic hydrogen evolution tests. After 4 h the evolved H_2 gas was measured collecting 200 μL of gas using an air-tight syringe (Hamilton) from the headspace of the reactor and analyzing it in a gas chromatograph (GC, Thermo Scientific TRACE 1300-GC, N_2 carrier). The irradiance (mW cm^{-2}) for each specified wavelength (300, 350, 420, 450, 500, and 600 nm) was measured at the location of the cell using a light source consisting of a 1000 W Xe lamp (LSH602) and a monochromator (MSW306, LOT-Quantum Design). A compact power and energy console (PM100D, Thorlabs) connected to a photodiode power sensor (S130VC, Thorlabs) was utilized for these measurements. Additionally, the spectrum for each wavelength was assessed using a spectral luminance meter (SRI-RL-5000UV, Allied Scientific). The quantum efficiency was calculated using the following equation (eqn (1)):

$$\mathrm{AQE}\,(\%) = \frac{2 \times \text{number of the hydrogen molecules}}{\text{number of the incident photons}} \quad (1)$$

The irradiance of each specified wavelength in the monochromator were 10.3, 18.4, 20.15, 21.3, 29, and 23.9 mW cm^{-2} for 300, 350, 420, 450, 500, and 600 nm, respectively. The detailed data regarding the calculations are provided in the ESI.† The emission spectra for each wavelength are shown in Fig. S1.†

2.7. Photoelectrochemical performance measurements

The transient photocurrent responses of the synthesized materials without external bias were measured using an electrochemical workstation (AUTOLAB PGSTAT 204, METROHM). A three-electrode electrochemical cell was configured, using Ag/AgCl (3.5 M KCl) as the reference electrode and a platinum wire as the counter electrode. The working electrode was prepared using the following procedure: 5 mg of catalyst were dispersed in 30 μL of Nafion, 210 μL of ethanol, and 70 μL of water to create a uniform suspension. The suspension was stirred for 2 hours and sonicated for 10 minutes. Subsequently, 18 μL of the suspension was applied to FTO glass on a heating plate set at 50 °C. The paste was deposited on the FTO glass (transmittance: 82%, resistance: 7 ohm sq^{-1}, dimensions: 2 cm × 0.5 cm × 0.22 cm, 3D Nano, Poland) using a drop-casting method over an area of 1 cm × 0.5 cm, whereas the remaining half of the FTO area was covered with duct tape. The electrodes were immersed in a 0.1 M Na_2SO_4 electrolyte solution within a Teflon-lined photoreactor featuring a 1 cm diameter window. Finally, the working electrode was irradiated using a 150 W Xe lamp (E7536, HAMAMATSU PHOTONICS K. K.), equipped with a water filter to eliminate IR irradiation and a shutter.

3. Results and discussion

3.1. XRD analysis

In Fig. 2 the XRD patterns of NiAl, ZIS, and ZIS/NiAlx (x = 12, 25, 50) heterostructures can be seen.

The pristine NiAl sample exhibits peaks at 11.4°, 22.9°, 34.5°, 39.0°, 46.2°, 60.2°, 62.6° that correspond to planes (003), (006) (012), (015), (018), (110), and (113), respectively, and belong to rhombohedral crystal system[26,27] Pure ZIS, by contrast, has peaks at 21.5°, 26.7°, 27.6°, 30.4°, 45.7°, 47.1°, and 52.4° attributed to planes (003), (100), (011), (012), (105), (110), and (113), which belong to the hexagonal crystal system.[28–30] Overall, ZIS crystals in hexagonal phase in our study additionally might contain sulfur intermediates due to

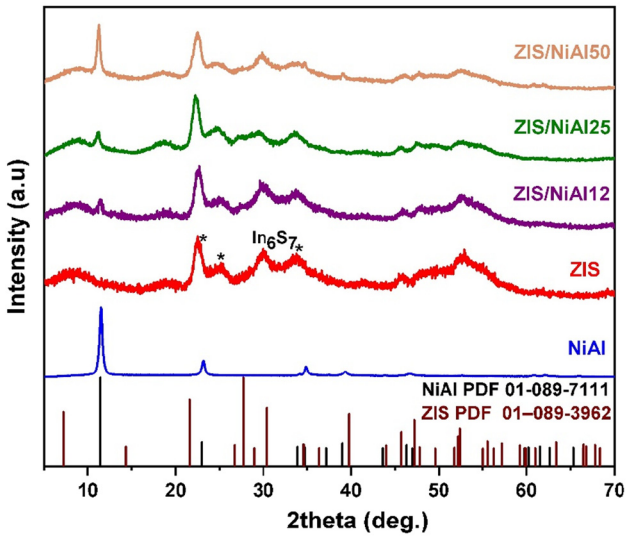

Fig. 2 XRD pattern of NiAl, ZIS, and ZIS/NiAl*x* (*x* = 12, 25, 50) heterostructures.

the pH adjusted to 2.5 by 0.1 M H_2SO_4 aqueous solution. Considering this, pH of the synthesis condition can be considered suitable for the metal cation availability for the ZIS synthesis. Although the Zn^{2+} : In^{3+} molar ratio was set to the ideal stoichiometry (1 : 2) for ZIS formation, our results and prior studies show that this alone is insufficient to ensure phase purity. Given the influence of precursor hydrolysis kinetics, sulfur release timing, and the pH-sensitive reactivity of the metal ions, it is likely that indium-rich secondary phases such as In_6S_7 (peaks at 22.5; 25° and 33.8°) are also present in our samples.[30,31] Sigl *et al.*, prepared ZIS thin film as well as the powdered ZIS samples. They mentioned in their samples that in In-rich samples (with Zn : In molar ratios of *e.g.* 1 : 2.2), In_2S_3 was formed in considerable amounts in addition to the ZIS phase.[32] Even the sample with ideal stoichiometric molar ratio (1 : 2.0 Zn : In) formed ZIS crystals that are assigned to hexagonal ZIS phase, but several weak reflections are absent. In all ZIS/NiAl*x* composites, a peak at 11.4° appears, confirming the formation of a heterostructure between ZIS and NiAl, thus indicating their successful combination; as the amount of NiAl increases, the peak becomes more prominent.

3.2. Morphology

In Fig. 3(a)–(c), the SEM images of the ZIS, NiAl, and ZIS/NiAl25/1.95Pt samples are presented. As shown in Fig. 3(a), the SEM image of pristine ZIS reveals aggregates with irregular shapes and a porous surface texture. These structures display a tendency to form clusters and agglomerates, which is a known characteristic of ZIS due to its layered morphology. This porous nature may facilitate the diffusion of reactants and enhance photocatalytic activity. During the hydrothermal synthesis of pristine ZIS, thioacetamide undergoes gradual thermal hydrolysis, releasing S^{2-} ions that react with Zn^{2+} and In^{3+} to form ZIS *via* homogeneous nucleation. In Fig. 3(b), the NiAl-LDH exhibits a distinct and well-organized flower-like morphology, with microflowers ranging from approximately 2 to 5 μm in diameter. These structures consist of radially aligned nanosheets, forming three-dimensional architectures that significantly increase the surface area. The formation of NiAl-LDH during hydrothermal synthesis involves the slow hydrolysis of urea, which gradually increases the pH and allows controlled co-precipitation of Ni^{2+} and Al^{3+} as layered hydroxide sheets. Fluoride ions from NH_4F assist in morphological regulation, while carbonate ions generated from urea act as charge-balancing interlayer anions. These processes lead to the self-assembly of flower-like NiAl-LDH microspheres composed of ultrathin nanosheets. This morphology results from a balance of nucleation, growth kinetics, and the presence of F^- ions, which can act as structure-directing agents by selectively adsorbing on specific crystal faces. A similar flower-like morphology of NiAl-LDH, composed of nanosheet assemblies, was also reported in a recent study on NiAl-LDH/CeO_2 heterojunctions, where it contributed to enhanced interfacial contact and photocatalytic performance.[33] In the composite ZIS/NiAl25/1.95Pt (Fig. 3(c)), both morphologies are present: the flower-like NiAl-LDH structures are interspersed within the ZIS aggregates, indicating successful heterojunction formation. The intimate contact between the two components suggests effective interfacial charge transfer. During the *in situ* synthesis of ZIS/NiAl-LDH composites, the presence of NiAl-LDH nanosheets in acidic medium facilitates heterogeneous nucleation and oriented growth of ZIS nanostructures. Thioacetamide acts as a slow sulfur source, enabling controlled reaction of Zn^{2+} and In^{3+} with S^{2-} under mild hydrothermal conditions. Electrostatic attraction and surface compatibility between ZIS and NiAl-LDH promote tight interfacial contact, leading to the formation of a 2D–2D heterostructure with enhanced interfacial charge transfer properties.

In Fig. 3(d) and (e), the HRTEM images of the ZIS/NiAl25/1.95Pt sample are shown. In these images, the lattice fringes of 0.320 and 0.292 nm, attributed to planes (011) and (012), respectively, belong to ZIS. Additionally, the lattice fringes of 0.284 and 0.299 nm were also observed, corresponding to plane (−202) of platinum hydrogen oxide (PDF 71-2466) and plane (100) of platinum oxide (PDF 27-1331), respectively. The Pt particle size distribution was estimated by measuring the dimensions of nanoparticles from various HRTEM images, with the average value calculated based on measurements of 130 nanoparticles. The as-deposited nanoparticles display a narrow size distribution (Fig. 3f), with sizes ranging from 0.8 to 2.9 nm and an average size of d_{Pt} = 1.71 ± 0.04 nm. EDX mapping and EDX data confirm the presence of Ni, Al, Zn, In, S, and Pt elements in the ZIS/NiAl25/1.95Pt sample (Fig. S2(a) and (b)†), further confirming the Pt photodeposition on the ZIS/NiAl25 substrate.

3.3. FT-IR and Raman analysis

The FTIR spectra of bare NiAl-LDH, ZIS and the composites ZIS/NiAl*x* can be seen in Fig. 4(a). For pure NiAl, the peaks at around 3552 and 1644 cm^{-1} are attributed to the hydroxyl

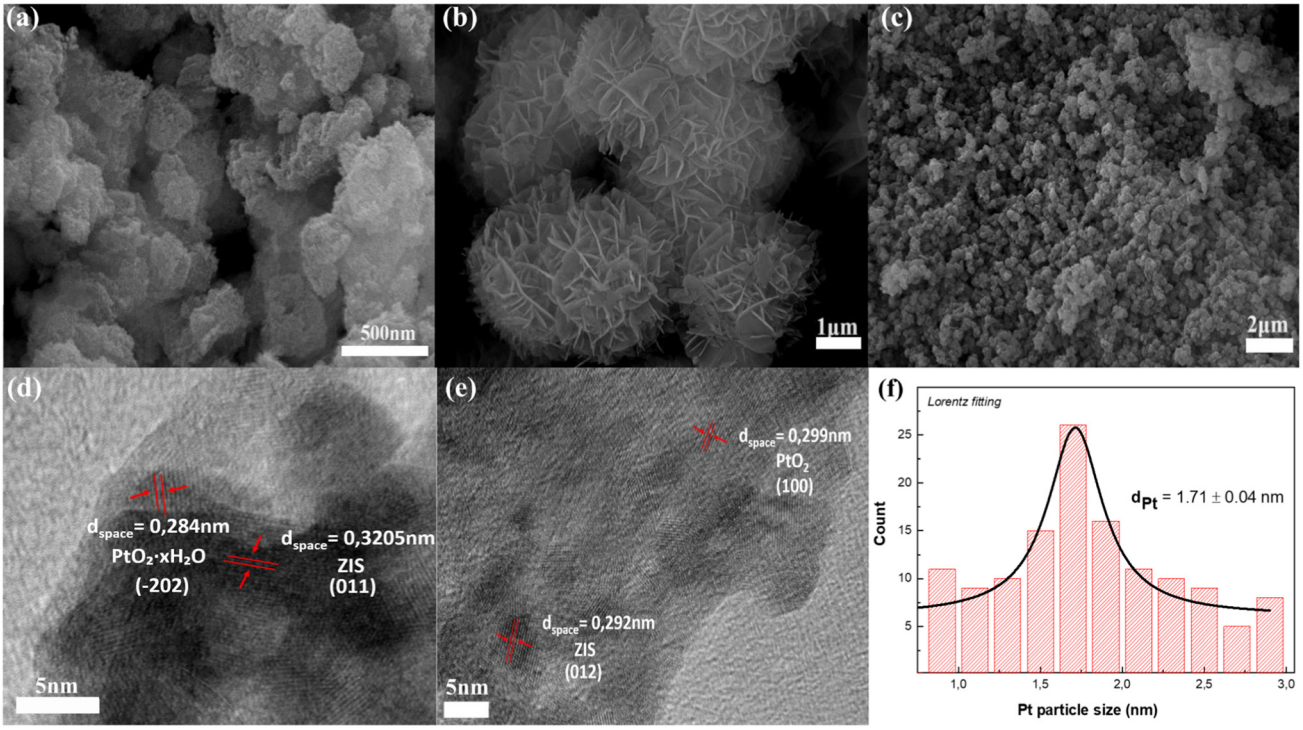

Fig. 3 (a) SEM images of ZIS; (b) NiAl; (c) ZIS/NiAl25/1.95Pt; (d) and (e) HRTEM images of the ZIS/NiAl25/1.95Pt sample; (f) particle size distribution of photodeposited Pt nanoparticles on the ZIS/NiAl25/1.95Pt sample.

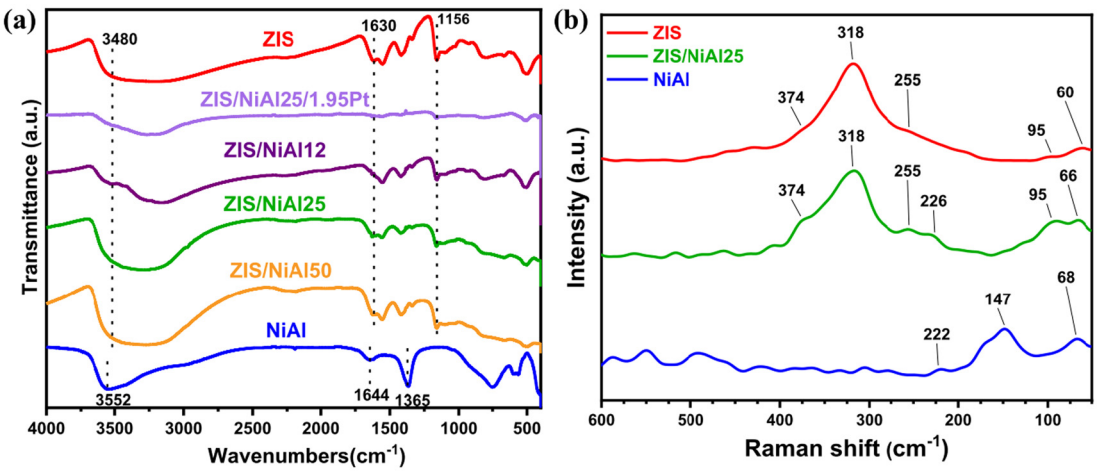

Fig. 4 (a) FTIR spectra of NiAl, ZIS/NiAl*x*, *x* = 12, 25, and 50, ZIS/NiAl25/1.95Pt and ZIS (b) Raman spectra of NiAl, ZIS/NiAl25, and ZIS.

groups and water molecules absorbed on the surface, specifically the stretching and bending vibrations of interlayer and surface (O–H) water molecules.[34,35] Additionally, the peak at 1365 cm^{-1} indicates the stretching vibrations of interlayer carbonate groups CO_3^{2-}. Signals below 800 cm^{-1} correspond to lattice vibrations of the cation layer of the LDH either M–O or M–O–M, where M = Ni or Al.[36] For pristine ZIS the broad band at around 3480 cm^{-1} is owing to hydroxyl groups and the peaks located at around 1630 cm^{-1} and 1156 cm^{-1} are characteristic peaks for this material. Notably, the composite materials ZIS/NiAl*x* exhibit signals from the characteristic peaks of both their pristine components, indicating a successful combination. In the case of ZIS/NiAl25/1.95Pt sample, a decrease in the intensity of the bands originating from ZIS was observed. The photoreduction process used to deposit Pt may alter the surface chemistry of ZIS, further contributing to the weakening of its vibrational features.

The composite ZIS/NiAl25 was further analyzed using Raman spectroscopy, as presented in Fig. 4(b), with spectra of pristine ZIS and NiAl included for comparison. For the plain

ZIS sample, as observed from XRD analysis (Fig. 2), the spinel structure crystallizes in the hexagonal *P*3*m*1 (156) lattice where zinc atoms occupy tetrahedral T_d sites, whereas Indium atoms reside in the octahedral O_h sites, which coordinated with the C_{3v} symmetry. Consequently, five active Raman modes are anticipated for the sulfur atoms: one A_{1g}, one E_g, and three F_{2g} modes.[24,37] The resulting Raman spectra show that the A_{1g} mode appears at 374 cm^{-1} for the pristine ZIS and NiAl-ZIS composite as a shoulder of the F_{1u} transverse optical mode at 318 cm^{-1}, which arises from long-wavelength lattice vibrations. Two F_{2g} modes are also observed at 255 cm^{-1} and 95 cm^{-1}, with the latter exhibiting a shift compared with other reports, resembling that of the homologous $CdIn_2S_4$.[37] The expected E_g mode is not directly visible in the acquired spectra of either ZIS or NiAl-ZIS. Instead, a shifted rigid layer mode at 60 cm^{-1} is observed in the pristine sample, which shifts to a higher wavenumber (66 cm^{-1}) in the composite, likely owing to the presence of a NiAl peak at 68 cm^{-1}.[38] Additionally, peak observed in the Raman spectra of the NiAl-ZIS composite can be attributed to the presence of NiAl-LDH, located at 226 cm^{-1}, corresponding to symmetric tensile vibrations of the Ni–O bond.[35]

3.4. Optical properties

To inspect the optical and electronic behavior of the samples, diffuse reflectance UV-vis spectroscopy (DRS) was measured (Fig. 5). Pristine NiAl shows three distinctive broad absorption bands. The first band in the UV region at 200–300 nm is owing to ligand-to-metal charge transfer from the O 2p orbital to the Ni 3d t2g orbital.[39] The other two bands, located in the visible part of the spectrum at 300–500 and 500–800 nm are attributed to d–d transitions of Ni^{2+} ions in the octahedral field.[40] The peaks at 380 and 654 nm are associated with to spin-allowed transitions $^3A_{2g}(F) \rightarrow {}^3T_{1g}(P)$ and $^3A_{2g}(F) \rightarrow {}^3T_{1g}(F)$, respectively. However, the peaks at 420 and 742 nm corresponded to spin-forbidden transitions $^3A_{2g}(F) \rightarrow {}^1T_{2g}(D)$ and $^3A_{2g}(F) \rightarrow {}^1E_g(D)$.[40–42] The pure ZIS sample exhibited increased absorption in the UV range as its absorption band is located at wavelengths below 500 nm. Although the spectra of the composite ZIS/NiAl*x* samples mostly resemble pure ZIS owing to NiAl being the smallest component (with amounts of NiAl in different samples being 12.5, 25, and 50 mg), all samples exhibit the NiAl band at 654 nm. As the NiAl percentage increases, a slight blue shift is observed in the absorbance. Additionally, the ZIS/NiAl25/1.95Pt composite shows a blue shift compared with pure ZIS and a considerable increase in absorbance for wavelengths higher than 450 nm (Fig. S3†). The E_g values of NiAl LDHs and $ZnIn_2S_4$ are calculated to be 2.43 and 2.44 eV, respectively (Fig. S4†).

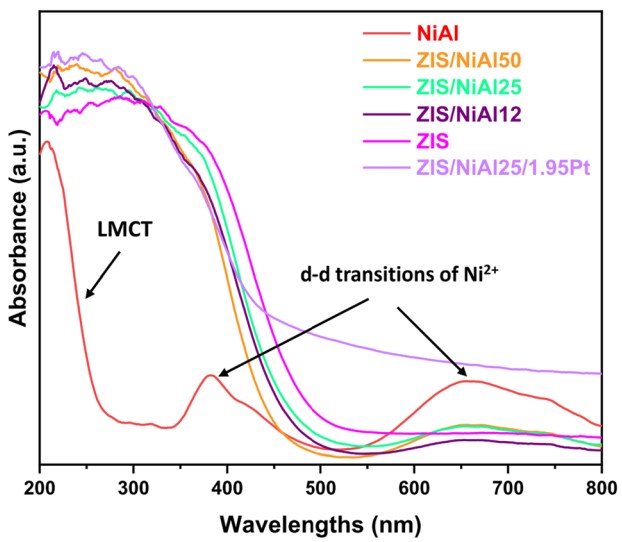

Fig. 5 DRS spectra of pristine NiAl, ZIS, ZIS/NiAl*x* composites, and ZIS/NiAl25/1.95Pt.

3.5. Photoluminescence properties

To draw conclusions about the transfer and recombination rates of photogenerated carriers, PL measurements were employed. A high photoluminescence (PL) intensity indicates an increased recombination rate of photogenerated carriers, whereas a lower intensity is expected to favor the photocatalytic process. Among the three different NiAl concentrations in ZIS/NiAl*x* composites, ZIS/NiAl25 exhibited the lowest signal (Fig. S5†). PL spectra exhibit reduced intensity in the composite materials loaded with Pt, indicating efficient separation and accelerated transfer of photo-induced charge carriers at the composite surface (Fig. 6b). Overall, this quenching behavior confirms the excited-state interaction between the Pt and ZIS/NiAl25 samples, demonstrating that the majority of excited electrons were transferred from ZIS/NiAl to Pt. Consequently, the composites loaded with Pt show improved photocatalytic performance for hydrogen production.

3.6. Photocurrent responses

The transient photocurrent responses of the ZIS, NiAl, ZIS/NiAl25, and ZIS/NiAl25/1.95Pt samples are depicted in Fig. 7. Pristine NiAl and ZIS exhibit lower signals owing to high recombination rates, which is expected since these two components suffer from charge recombination. By contrast, the ZIS/NiAl25 heterostructure shows a considerably enhanced response compared with ZIS and NiAl LDHs, indicating that the construction of the ZIS/NiAl25 heterojunction can improve charge transfer. However, the sample with the photodeposited Pt nanoparticles (ZIS/NiAl25/1.95Pt) did not display a higher signal than ZIS/NiAl25, despite showing considerably enhanced H_2 generation. This discrepancy likely arises because the improved performance is owing to the increase in active sites provided by the Pt nanoparticles, rather than enhanced charge dissociation.

The pristine ZIS sample exhibits a relatively stable photocurrent during each light-on/off cycle. In contrast, the ZIS/NiAl25 composite shows a higher initial photocurrent response. However, its photocurrent response dropped by around 50% at the end of the light-on/off interval cycle, but

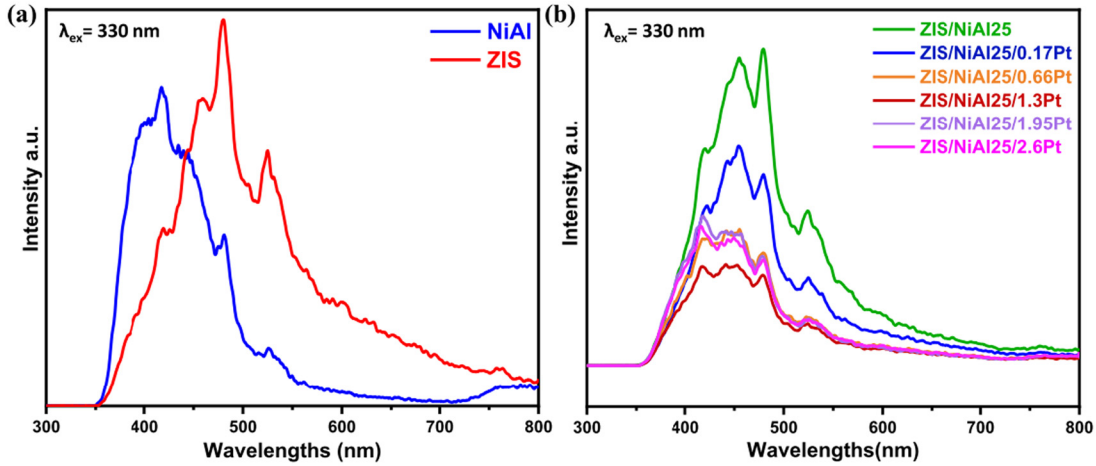

Fig. 6 PL spectra of (a) ZIS, NiAl and (b) ZIS/NiAl25 with different Pt loadings.

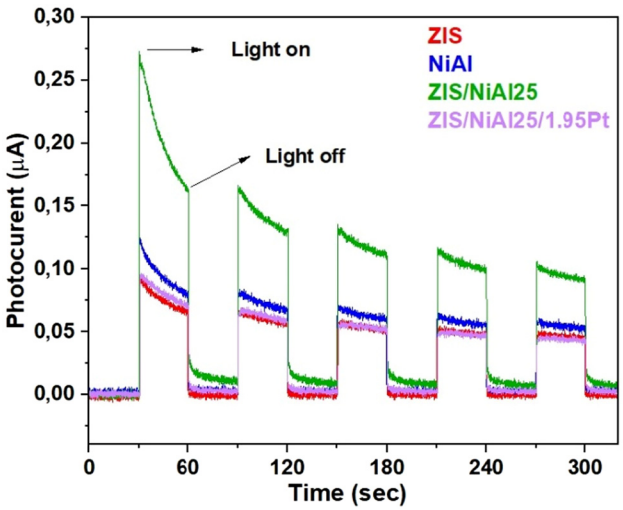

Fig. 7 Transient photocurrent responses of ZIS, NiAl, ZIS/NiAl25, and ZIS/NiAl25/1.95Pt.

still the photocurrent response was higher than that of pristine ZIS. This indicates that more efficient generation and separation of charge carriers due to the formation of a type-II n–n heterojunction in ZIS/NiAl25. Overall, pristine ZIS shows greater stability than ZIS/NiAl25, while its photocurrent response is lower compared to that of ZIS/NiAl25. This gradual decline in the photocurrent amplitude by ZIS/NiAl25 across cycles may originate from the progressive structural degradation or excessive photooxidation in NiAl under continuous operation. On the other hand, the ZIS/NiAl25/1.95Pt sample exhibits the most stable and consistent photocurrent response, despite lower photocurrent response value thanZIS/NiAl25. The higher stability can be explained by the incorporation of Pt as a cocatalyst not only facilitates interfacial electron trapping but also enhances the long-term photochemical stability of the composite system. While the competitive electron mobility between the counter electrode and working electrode in the photoelectron chemical or light shielding effect by the Pt deposition might be responsible for the declined photocurrent response in ZIS/NiAl25/1.95Pt in comparison with the ZIS/NiAl25. It is noteworthy that the Pt loading on the TiNTs or g-C_3N_4/TiNTs led to an obviously decreased UV response compared with the bare TiNTs and g-C_3N_4/TiNTs.[43] Zare *et al.* showed that the transient photocurrent density is decreasing with increasing Pt content of the electrodes and in pure nanotube arrays (TNA) is higher than Pt/TNAs.[44] On the other hand, excessive Pt deposition can negatively affect the photoresponse of the photocatalytic system. For instance, the Pt2.0 sample exhibits a lower photocurrent compared to the Pt1.0 sample. This could be attributed to the excessive Pt loading, which may block light absorption and act as a recombination center for photogenerated electron–hole pairs.[45]

3.7. XPS analysis

The XPS spectra of the chemical elements for the ZIS/NiAl25/1.95Pt_fresh and ZIS/NiAl25/1.95Pt_used samples are presented in Fig. 8. In Fig. 8a, the high-resolution Zn 2p spectrum displays a peak centered around 1022.2 eV, which is consistent with Zn $2p_{3/2}$.[46] The In 3d XPS spectrum of ZIS/NiAl25/1.95Pt (Fig. 8b) shows binding energies at 445.2 and 452.8 eV, corresponding to In $3d_{3/2}$ and In $3d_{5/2}$, respectively. The S 2p XPS spectrum (Fig. 8c) exhibits two main peaks located at 161.9 and 163.1 eV, in agreement with S $2p_{3/2}$ and S $2p_{1/2}$, respectively.[47,48] Meanwhile, in the Ni 2p spectrum (Fig. 8d), the peak at 857 eV is primarily attributed to the presence of Ni $2p_{3/2}$. The Al 2s spectrum (Fig. 8e) reveals a signal centered at 118.5 eV in the ZIS/NiAl25/1.95Pt sample.[49] In the Pt 4f spectrum (Fig. 8f), two signals centered at 75.8 and 72.5 eV correspond to Pt $4f_{5/2}$ and Pt $4f_{7/2}$, respectively. The position of the Pt $4f_{7/2}$ peak at 72.5 eV suggests that platinum is present in the samples as $Pt(OH)_2$.[50,51] XPS analyses were conducted on ZIS, NiAl, ZIS/NiAl25 (fresh and used in PHE), and ZIS/NiAl25/1.95Pt (fresh and used in PHE). The term "used" refers to samples that underwent stability testing in the PHE, whereas

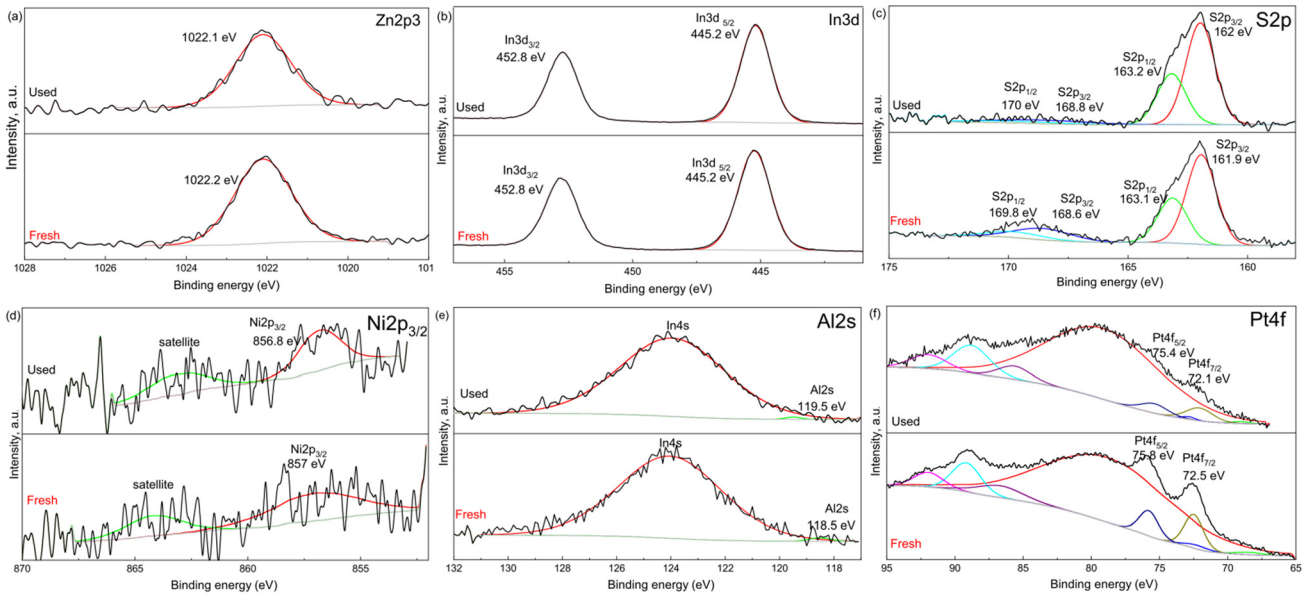

Fig. 8 High resolution XPS spectra of the fresh and used ZIS/NiAl25/1.95Pt, of the (a) zinc (b), indium (c), sulphur (d), nickel (e), aluminum (f), platinum.

"fresh" denotes samples after synthesis. The survey XPS pattern (Fig. S6†) confirms that fresh and used ZIS/NiAl25/1.95Pt consist of Zn, In, S, Ni, Al, Pt, C, and O elements. Table 1 presents the elemental composition of the surface layer for NiAl, ZIS, ZIS/NiAl25 (fresh and used), and ZIS/NiAl25/1.95Pt (fresh and used).

Notably, the samples after the process contained a higher amount of carbon than the fresh sample likely owing to the presence of the scavenger (TEOA) on the surface of the used photocatalyst. The carbon content on the surface of the ZIS/NiAl25 photocatalysts was measured at 8.9 at% for the fresh sample and 82.3 at% for the used sample. In the case of the ZIS/NiAl25/1.95Pt sample, the carbon content was 7.0 at% for the fresh sample and 27 at% for the sample after the photocatalytic stability test. Additionally, the ZIS/NiAl25/1.95Pt sample after processing exhibited a considerably lower platinum content than the fresh sample. After each experiment, the reaction solution was centrifuged to recover the photocatalyst, which was then washed four times with water and once with ethanol before being dried for the next cycle. This procedure may have led to leaching and a decrease in the platinum mass on the surface of the photocatalyst. Notably, upon comparing these spectra, the positions of the XPS peaks did not change after the photocatalytic process (the values of the binding energy are indicated next to the peaks). Therefore, in conclusion, the chemical states of the elements remained the same, thus confirming the stability of the studied ZIS/NiAl25/1.95Pt sample.

3.8. Photocatalytic H_2 production

The photocatalytic H_2 production rates of pristine samples ZIS, NiAl, and the formed heterostructures ZIS/NiAl*x*/*y*Pt were tested under UV-vis and visible irradiation ($\lambda > 420$ nm) using TEOA as a sacrificial agent. In all samples, the generated H_2 increased linearly and progressively, indicating continuous H_2 formation throughout the entire 4-hour catalytic reaction process.

Photoactivity under UV-vis irradiation. In Fig. 9(a) and (b), the results under UV-vis irradiation are depicted. The H_2 rates of pure ZIS and NiAl are considerably lower than those of their combination in the ZIS/NiAl*x* heterostructures.

Table 1 Elemental composition of the studied samples (at%)

	Elemental composition (atomic %)							
Sample label	C	O	Ni	Al	Zn	In	S	Pt
NiAl	8.0	60	14.3	17.7	0	0	0	0
ZIS	9.5	47	0	0	1.5	28.5	13.5	0
ZIS/NIAl25_fresh	8.9	48.8	1.8	0.6	2.5	26.7	10.7	0
ZIS/NIAl25_used	82.3	14.8	0.15	0.4	0.1	1.36	0.8	0
ZIS/NiAl25/1.95Pt_fresh	7.0	51.3	0.3	0.16	2.1	27.8	11	0.4
ZIS/NiAl25/1.95Pt_used	27.0	44.5	0.16	0.1	0.74	22.9	4.4	0.16

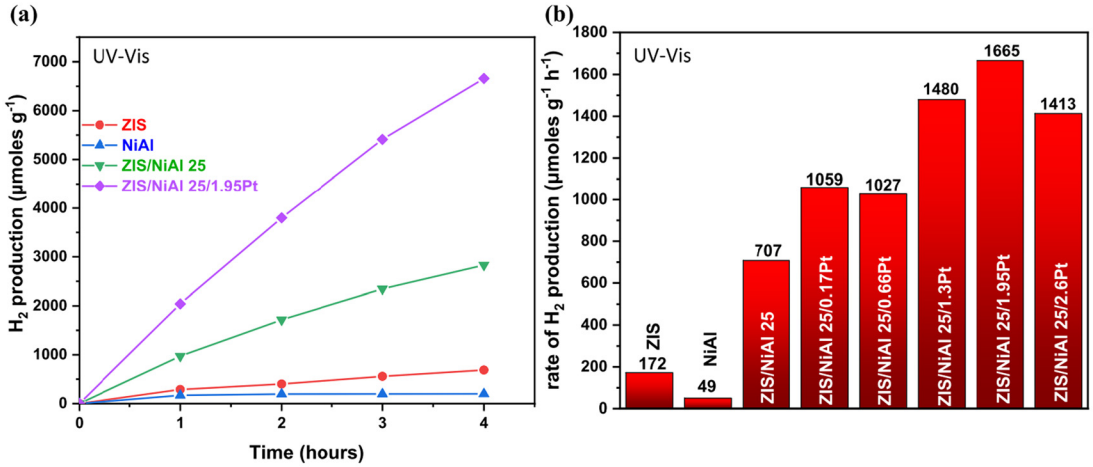

Fig. 9 Photocatalytic H_2 production (a) and rate (b) of ZIS, NiAl, ZIS/NiAl25, and ZIS/NiAl25/*y*Pt under UV-vis irradiation. Reaction conditions: 25 mg of catalyst, 20 mL of aqueous solution, 10% v/v sacrificial agent (TEOA), and Xe lamp 1000 Watt.

Despite all ZIS/NiAl*x* heterostructures enhancing H_2 production, the optimal amount of NiAl was found to be 25 mg (Fig S7†), which exhibited a rate of 4.1 times higher (707 μmol g^{-1} h^{-1}) than that of pristine ZIS (172 μmol g^{-1} h^{-1}). The explanation for the enhanced activity of ZIS/NiAl*x* samples is that the formation of heterostructures is a common strategy to address insufficient charge migration and separation.[52,53] For the Pt loading on the ZIS/NiAl25 sample, the optimal loading was 1.95 wt% Pt (ZIS/NiAl25/1.95Pt), resulting in an H_2 production rate of 1665 μmol g^{-1} h^{-1}, which is 2.35 times higher than that of ZIS/NiAl25 and 9.6 times higher than that of pure ZIS under UV-vis irradiation. The enhanced H_2 production of Pt-loaded samples is expected, as noble metals, especially Pt with a work function of 5.65 eV,[54] when in close contact with a semiconductor, exhibit electron trapping properties and simultaneously act as active sites.[55] Interestingly, the data from comparative experiments between ZIS/NiAl25 and ZIS/NiAl25/1.95Pt samples with P25 and P25/1.95Pt, respectively (Fig. S8†), showed that the ZIS/NiAl25 sample had a rate of 2.35 times higher than P25 (708 μmol g^{-1} h^{-1}) and ZIS/NiAl25/1.95Pt exhibited a rate very similar to P25/1.95Pt (1666 μmol g^{-1} h^{-1} for our sample and 1758 μmol g^{-1} h^{-1} for P25/1.95Pt). Additionally, the photocatalytic activity of the samples was tested to check the repeatability of the synthesis. The photocatalytic H_2 rates of different batches for ZIS/NiAl25 and ZIS/NiAl25/1.95Pt under UV-vis are shown in Fig. S9.† This experiment confirmed that the samples obtained according to the procedure described in this publication are highly reproducible.

Photoactivity under visible irradiation. In Fig. 10(a) and (b), the H_2 rates of the samples are shown under visible irradiation (λ > 420 nm). The ZIS/NiAl25 sample exhibited a rate that was 4.8 times higher than its pure component, ZIS, with the rates of 231 and 48 μmol g^{-1} h^{-1}. The optimum metal loading was

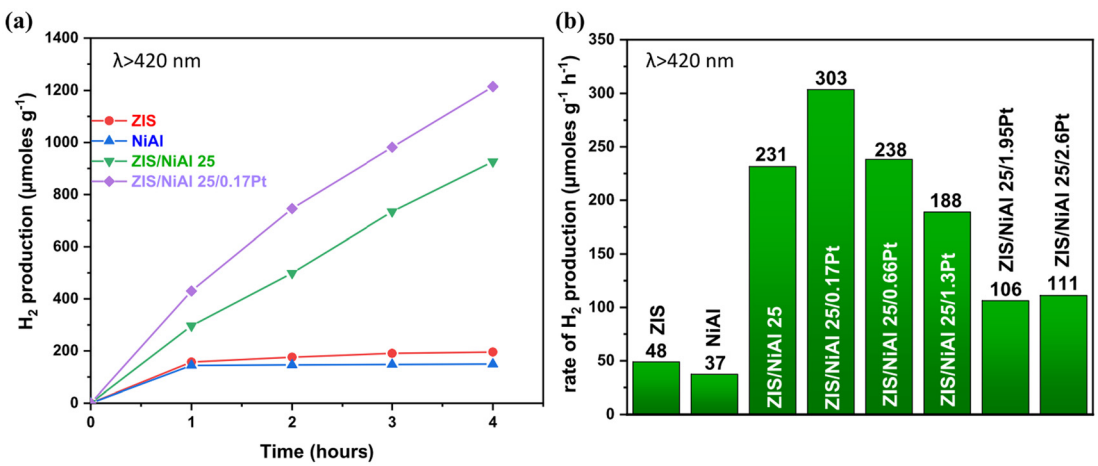

Fig. 10 Photocatalytic H_2 production (a) and the rate (b) of ZIS, NiAl, ZIS/NiAl25, and ZIS/NiAl25/*y*Pt under visible irradiation. Reaction conditions: 25 mg of catalyst, 20 mL aqueous solution, 10% v/v sacrificial agent (TEOA), Xe lamp 1000 Watt, and λ > 420 nm.

0.17 wt% Pt (ZIS/NiAl25/0.17Pt), which demonstrated a rate of 1.3 times higher than ZIS/NiAl25 and 6.3 times higher than ZIS.

The different behavior of these systems under UV-vis and visible irradiation is noteworthy as the optimal Pt loading for UV-vis is the highest (1.95 wt%), whereas for visible it is the lowest (0.17 wt%). Nevertheless, in both cases, further addition of Pt beyond the optimum loading is disadvantageous as the excess Pt nanoparticles act as recombination centers or excessively cover the surface of the semiconducting substrate, preventing it from being sufficiently activated to produce photogenerated carriers. To verify that the best results under both types of irradiation could be achieved only through the interaction of the heterostructure ZIS/NiAl25 and Pt, supplementary experiments were conducted with ZIS/*y*Pt and NiAl/*y*Pt, where y = 1.95 or 0.17, the optimal Pt loading for each case, as illustrated in Fig. S10 and S11.†

Stability test. The stability tests are shown for the most active photocatalysts in Fig. 11. After each experiment, the reaction solution was centrifuged to retrieve the photocatalyst, which was washed with water four times and with ethanol once. A fresh solution was then prepared and purged for the next cycle. The ZIS/NiAl25 sample shows only a 2% drop in hydrogen evolution activity over four cycles, in contrast to a 24% drop for pure ZIS. This clearly indicates that NiAl-LDH enhances the photostability of the heterojunction, likely by mitigating the photocorrosion tendency of ZIS through improved charge separation and sacrificial agent oxidation.

Under UV-vis light, the ZIS/NiAl25/1.95Pt sample retained 71% of its initial H_2 production after four consecutive cycles. Although almost 30% drop was observed in H_2 production from the first to the second cycle, the decrease in subsequent cycles was much milder. This decline can be attributed to the loss of some Pt from the surface of the photocatalyst, as confirmed by XPS data (Fig. 12 and Table 1).

The Pt content on the surface of ZIS/NiAl25/1.95Pt was 0.4 and 0.16 at% for the fresh and used samples, respectively. This decrease most likely results from partial loss of Pt from the photocatalyst surface during the photocatalytic process, where Pt nanoparticles may detach or leach into the solution. Such loss mechanisms are common in noble-metal-loaded photocatalysts operated under aqueous and illuminated conditions. In addition, it is important to note that between each photocatalytic cycle, the sample was separated from the solution by centrifugation and thoroughly washed (four times with water and once with ethanol) before reuse. While necessary to eliminate residual reactants or intermediates, this recovery procedure may also contribute to mechanical removal or partial loss of weakly bound Pt species, further affecting surface Pt content. By contrast, the ZIS/NiAl25 catalyst exhibited remarkable stability, with only a slight 2% drop in H_2 production detected. Thus, NiAl serves as a stabilizing component in the photocorrosion process occurring in ZIS (24% drop in H_2 production after four cycles).[8] Under visible light, the optimum catalyst (ZIS/NiAl25/0.17Pt) in the second cycle retained 61% of its initial H_2 production. No further cycles were conducted for this sample as the H_2 production in the second cycle was lower than that of the sample without Pt (ZIS/NiAl25) (Fig. S12†).

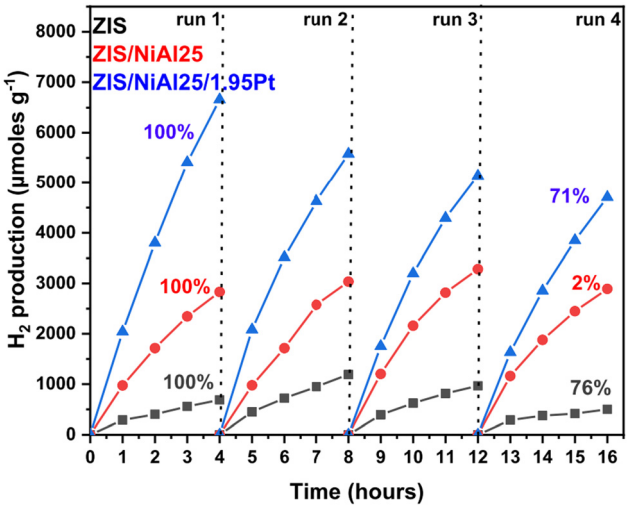

Fig. 11 Cycling study of ZIS, NiAl, and ZIS/NiAl/1.95Pt under UV-vis light. Reaction conditions: 25 mg of catalyst, 20 mL aqueous solution, 10% v/v of sacrificial agent (TEOA), and Xe lamp 1000 Watt.

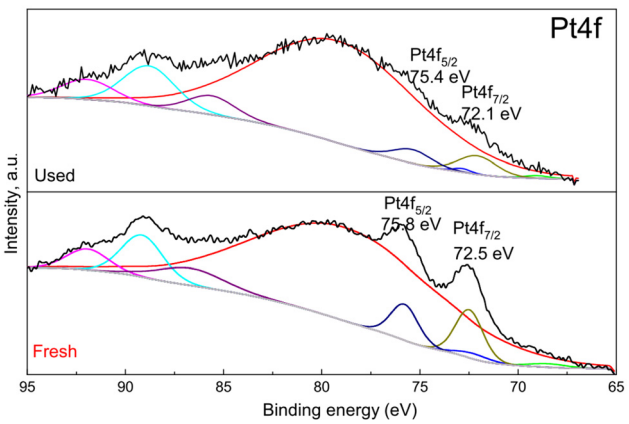

Fig. 12 XPS spectra of Pt4f for fresh and used ZIS/NiAl25/1.95Pt.

Action spectra analysis. The apparent quantum efficiency (AQE) of the optimal photocatalyst ZIS/NiAl25/1.95Pt was measured at six different wavelengths, ranging from 320 to 600 nm (Table S2†). The AQE values for each wavelength closely followed the absorbance spectrum of the sample (Fig. 13), with the highest value recorded at 320 nm, yielding an AQE of 1.7%. For visible light (420 nm), the AQE reached 0.3%.

3.9. Photocatalytic mechanism

The valence band (VB) positions, determined *via* valence band XPS, were found to be +1.7 eV for ZIS and +1.0 eV for NiAl-LDH *versus* the normal hydrogen electrode (NHE) (Fig. S13†). In addition, based on the optical band gap energies obtained from the UV-vis diffuse reflectance spectra (Fig. S4†), which

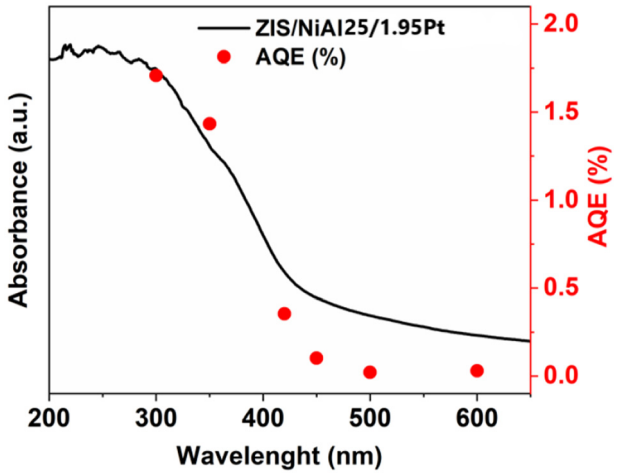

Fig. 13 AQE of H_2 evolution at corresponding wavelength for ZIS/NiAl25/1.95Pt sample.

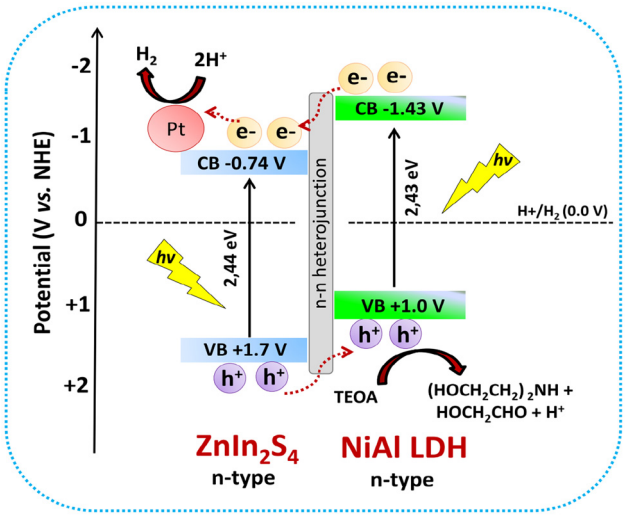

Fig. 14 Proposed mechanism of photocatalytic H_2 generation in the presence of $ZnIn_2S_4$/NiAl-LDH/Pt n–n heterojunctions under UV-vis irradiation.

are 2.44 eV for $ZnIn_2S_4$ and 2.43 eV for NiAl-LDH, the conduction band (CB) positions were calculated using the equation $E_{CB} = E_{VB} - E_g$. Applying this relation, the CB position for $ZnIn_2S_4$ was determined to be −0.74 eV (*i.e.*, +1.7 eV–2.44 eV), and for NiAl-LDH it was −1.43 eV (*i.e.*, +1.0 eV–2.43 eV), both relative to the normal hydrogen electrode (NHE). Thus, the CB potentials of ZIS and NiAl-LDH are thermodynamically suitable for PHE when considering the H^+/H_2 reduction potential of 0 eV (V *vs.* NHE). $ZnIn_2S_4$ and NiAl-LDH exhibit n-type semiconductor properties (with excess electrons[9]). In this type II staggered n–n heterojunction, the charge transfer process is driven by the differences in the conduction band energies of the two n-type materials. The conduction band (CB) of ZIS is more positive than that of NiAl-LDH, facilitating the separation of charge carriers. This separation is advantageous because the diffusive driving force for the charge carriers arises from the well-aligned band potentials of the two semiconductors, resulting in the formation of a robust heterojunction interface. Based on these findings, a photocatalytic mechanism for the ZIS/NiAl-LDH/Pt composite under UV-vis irradiation has been proposed (Fig. 14). During UV-vis irradiation, ZIS and NiAl-LDH are photoexcited, producing photogenerated electrons (e^-) and holes (h^+) in the CB and VB, respectively.

The photogenerated electrons in the CB of NiAl-LDH can transfer across the n–n heterojunction into the CB of ZIS, where they are captured by the active sites of ZIS/NiAl/Pt. This configuration facilitates the spatial separation of photogenerated electron–hole pairs: electrons from NiAl-LDH migrate to the CB of ZIS, while holes transfer to the VB of NiAl-LDH. This directional migration reduces recombination and prolongs charge carrier lifetimes, as further supported by PL quenching and enhanced transient photocurrent responses (Fig. 6 and 7). Improving charge separation is key for boosting photocatalytic hydrogen evolution. Moreover, a recent study by Yang *et al.* showed that a flower-like NiAl-LDH/CeO_2 hybrid heterojunction with a well-designed S-scheme interface exhibited enhanced charge separation and photocatalytic performance due to strong interfacial coupling and internal electric field effects.[33] Recent studies have demonstrated that internal electric fields, such as dipole fields induced by atomic asymmetry in amorphous ZnCdS, can serve as powerful driving forces for carrier separation[56]

The Pt nanoparticles act as electron sinks for H_2 generation by capturing the photogenerated electrons and preventing recombination. Additionally, the role of noble metal nanoparticles (NMNPs) is not only to capture electrons but also to create sites for efficient H^+ ion reduction. Therefore, in conclusion, H_2 is generated on the surface of Pt NPs. As reported in the literature, platinum (Pt) stands out as the most effective cocatalyst for the hydrogen evolution reaction due to its high work function (5.40 eV relative to vacuum) and low overpotential. Consequently, the excellent photocatalytic hydrogen evolution (PHE) performance of the prepared composites can also be attributed to the presence of Pt, which significantly enhances the hydrogen evolution reaction. XPS analysis revealed that the Pt species primarily exist in the form of Pt $(OH)_2$, which functions as a co-catalyst by facilitating the hydrogen evolution reaction through efficient electron acceptance and promoting the reduction of protons. Moreover, regarding the HR-TEM findings, platinum can also exist in the form of platinum oxide. Compounds like PtO_2 and $Pt(OH)_2$ contribute to improved efficiency and stability in photocatalytic processes by promoting charge transfer, enhancing the activation of reactants, and participating in key reactions such as hydrogen evolution and oxidation. Holes generated in the valence band (VB) of ZIS are transferred through the n–n heterojunction to the VB of NiAl-LDH, effectively reducing the recombination of electron–hole pairs within ZIS. Furthermore, the holes that reach the surface of NiAl-LDH are captured by a sacrificial agent, such as triethanolamine (TEOA), which

boosts the photocatalytic performance. TEOA, present in the electrolyte, undergoes oxidation by these holes, as described in the outlined reaction mechanisms (reactions (1)–(4)).[57]

$$(HOCH_2CH_2)_2NCH_2CH_2OH \rightarrow (HOCH_2CH_2)_2N^{\bullet+}CH_2CH_2OH + e^- \quad (1)$$

$$(HOCH_2CH_2)_2N^{\bullet+}CH_2CH_2OH \rightarrow (HOCH_2CH_2)_2N^{\bullet}CHCH_2OH + H^+ \quad (2)$$

$$(HOCH_2CH_2)_2N^{\bullet}CHCH_2OH \rightarrow (HOCH_2CH_2)_2N^+ = CHCH_2OH + e^- \quad (3)$$

$$(HOCH_2CH_2)_2N^+ = CHCH_2OH + H_2O \rightarrow (HOCH_2CH_2)_2NH + HOCH_2CHO + H^+ \quad (4)$$

This oxidation process generates protons, which are subsequently reduced, leading to the production of hydrogen gas as observed in the photocatalytic system. In conclusion, NiAl-LDH plays a synergistic role by forming an efficient heterojunction with ZIS, enhancing charge separation, improving surface area, stabilizing the structure, and participating in hole transport and consumption.

4. Conclusion

$ZnIn_2S_4$ decorated with preprepared NiAl-LDH microflower-like structures was synthesized in an oil bath at 80 °C and modified using Pt photodeposition for the first time. It was demonstrated that the coupling of composite components considerably influenced the photocatalytic performance of the obtained hybrids. The effect of Pt deposition on ZIS/NiAl-LDH composites in PHE under UV-vis and visible (λ > 420 nm) irradiation was investigated. The introduction of an optimal amount of 0.17 wt% Pt on the surface of ZIS/NiAl25 increased the hydrogen production rate compared with bare ZIS by approximately 6.5 times under visible light irradiation. The optimal loading of NiAl and Pt (ZIS/NiAl25/1.95Pt) exhibited a considerably enhanced H_2 evolution rate of 1665 μmol g^{-1} h^{-1}, which is 9.6 times higher than that of pure ZIS under UV-vis irradiation. Furthermore, the ZIS/NiAl25 photocatalyst demonstrated exceptional stability over several cycles of the hydrogen generation process under UV-vis light. This improved PHE rate can be attributed to several following factors:

(i) The n–n heterojunction formed between ZIS and NiAl-LDH enhances both stability and photocatalytic performance by improving interfacial contact, facilitating efficient charge separation, minimizing electron–hole recombination, and broadening the light absorption range.

(ii) TEOA, serving as a hole scavenger, plays a vital role in hydrogen production by effectively suppressing charge carrier recombination.

(iii) PtO_2 and $Pt(OH)_2$ play substantial roles in enhancing the efficiency and stability of photocatalytic processes by facilitating charge transfer, improving reactant activation, and extending absorption ranges.

In conclusion, this work contributes to the development of innovative nanoscale solutions for energy sustainability, emphasizing the importance of rational design and environmental relevance in advancing photocatalytic technologies.

Author contributions

Anna P. Souri: investigation, methodology, visualization, data analysis, writing – original draft, and writing – review & editing. Onur Cavdar: investigation, methodology, data analysis. Maria Zografaki: investigation. Leila Zouridi: investigation. Vassilios Binas: writing – review & editing. Tomasz Klimczuk: investigation. Kostiantyn Nikiforow: investigation. Anna Malankowska: funding acquisition, visualization, conceptualization, methodology, investigation, visualization, data analysis, writing – original draft, and writing – review & editing. All authors have read and agreed to the published version of the manuscript.

Conflicts of interest

There are no conflicts to declare.

Data availability

Authors confirm that all relevant data supporting this article are included in the article and the ESI.†

Acknowledgements

Anna Malankowska acknowledges funding from the IDUB program, Poland (UGrant start 533-T000-GS57-24). Anna Souri acknowledges Daniel Fahrenheit Scholarship funded by the Mayor of Gdańsk, Poland. SEM images were obtained with the help of Stefanos Papadakis, TEM images were obtained with the help of Lambros Papoutsakis, and Raman measurements were taken with the help of Maria Androulidaki.

References

1 Y. Zhao, *et al.*, Layered Double Hydroxide Nanostructured Photocatalysts for Renewable Energy Production, *Adv. Energy Mater.*, 2016, **6**(6), 1–20, DOI: **10.1002/aenm.201501974**.

2 G. Zhang, *et al.*, A mini-review on $ZnIn_2S_4$-Based photocatalysts for energy and environmental application, *Green Energy Environ.*, 2022, **7**(2), 176–204, DOI: **10.1016/j.gee.2020.12.015**.

3 A. Hameed, M. Batool, Z. Liu, M. A. Nadeem and R. Jin, Layered Double Hydroxide-Derived Nanomaterials for Efficient Electrocatalytic Water Splitting: Recent Progress

and Future Perspective, *ACS Energy Lett.*, 2022, **7**(10), 3311–3328, DOI: **10.1021/acsenergylett.2c01362**.

4 J. Chen, C. Wang, Y. Zhang, Z. Guo, Y. Luo and C. J. Mao, Engineering ultrafine NiS cocatalysts as active sites to boost photocatalytic hydrogen production of MgAl layered double hydroxide, *Appl. Surf. Sci.*, 2020, **506**, 144999, DOI: **10.1016/j.apsusc.2019.144999**.

5 J. Guo, *et al.*, Photocatalytic degradation of persistent organic pollutants by Co-Cl bond reinforced CoAl-LDH/$Bi_{12}O_{17}Cl_2$ photocatalyst: mechanism and application prospect evaluation, *Water Res.*, 2022, **219**, 118558, DOI: **10.1016/j.watres.2022.118558**.

6 Y. Jiang, J. Guo, X. Li, G. Wu, M. Mu and X. Yin, Direct Z-Scheme 0D/2D heterojunction of CuO quantum Dots/ultrathin CoAl-LDH for boosting charge separation and photocatalytic CO_2 reduction, *Sol. Energy*, 2022, **231**, 705–715, DOI: **10.1016/j.solener.2021.12.001**.

7 G. Mishra, B. Dash and S. Pandey, Layered double hydroxides: A brief review from fundamentals to application as evolving biomaterials, *Appl. Clay Sci.*, 2018, **153**, 172–186, DOI: **10.1016/j.clay.2017.12.021**.

8 Z. Yang, S. Li, X. Xia and Y. Liu, Hexagonal MgAl-LDH simultaneously facilitated active facet exposure and holes storage over $ZnIn_2S_4$/MgAl-LDH heterojunction for boosting photocatalytic activities and anti-photocorrosion, *Sep. Purif. Technol.*, 2022, **300**, 121819, DOI: **10.1016/j.seppur.2022.121819**.

9 X. Deng, *et al.*, Carbon-Dots-Modified Hierarchical $ZnIn_2S_4$/Ni-Al LDH Heterojunction with Boosted Charge Transfer for Visible-Light-Driven Photocatalytic H_2 Evolution, *Inorg. Chem.*, 2023, **62**(24), 9702–9712, DOI: **10.1021/acs.inorgchem.3c01317**.

10 X. X. Jiang, *et al.*, Ultrathin sulfate-intercalated NiFe-layered double hydroxide nanosheets for efficient electrocatalytic oxygen evolution, *RSC Adv.*, 2020, **10**(21), 12145–12150, DOI: **10.1039/d0ra00845a**.

11 Z. Zhao, *et al.*, Multiple structural defects in ultrathin NiFe-LDH nanosheets synergistically and remarkably boost water oxidation reaction, *Nano Res.*, 2022, **15**(1), 310–316, DOI: **10.1007/s12274-021-3475-z**.

12 Z. Y. Zhao, X. Sun, H. Gu, Z. Niu, P. Braunstein and J. P. Lang, Engineering the Electronic Structures of Metal-Organic Framework Nanosheets via Synergistic Doping of Metal Ions and Counteranions for Efficient Water Oxidation, *ACS Appl. Mater. Interfaces*, 2022, **14**(13), 15133–15140, DOI: **10.1021/acsami.1c24170**.

13 C. Zheng, G. Jiang and Z. Jin, ZnCdS/NiAl hydrotalcite S-scheme heterojunction for efficient photocatalytic hydrogen evolution, *Int. J. Hydrogen Energy*, 2022, **47**(1), 292–304, DOI: **10.1016/j.ijhydene.2021.10.032**.

14 G. Gao, *et al.*, The construction of 3D hierarchical CdS/NiAl-LDH photocatalyst for efficient hydrogen evolution, *Int. J. Hydrogen Energy*, 2023, **48**(6), 2200–2210, DOI: **10.1016/j.ijhydene.2022.10.099**.

15 X. Deng, *et al.*, Carbon-Dots-Modified Hierarchical $ZnIn_2S_4$/Ni-Al LDH Heterojunction with Boosted Charge Transfer for Visible-Light-Driven Photocatalytic H_2 Evolution, *Inorg. Chem.*, 2023, **62**(24), 9702–9712, DOI: **10.1021/acs.inorgchem.3c01317**.

16 S. Zhao, *et al.*, In Situ Growth of $ZnIn_2S_4$ on MOF-Derived Ni-Fe LDH to Construct Ternary-Shelled Nanotubes for Efficient Photocatalytic Hydrogen Evolution, *Inorg. Chem.*, 2021, **60**(13), 9762–9772, DOI: **10.1021/acs.inorgchem.1c01064**.

17 Z. Yang, S. Li, X. Xia and Y. Liu, Hexagonal MgAl-LDH simultaneously facilitated active facet exposure and holes storage over $ZnIn_2S_4$/MgAl-LDH heterojunction for boosting photocatalytic activities and anti-photocorrosion, *Sep. Purif. Technol.*, 2022, **300**, 121819, DOI: **10.1016/j.seppur.2022.121819**.

18 S. Ma, X. Wang, K. Wan, B. Liu, Y. Yang and S. Wang, Metal-organic framework-derived $Zn_xCd_{1-x}S$/$ZnxCd_{1-x}$-MOF heterostructures promoting charge separation for photocatalytic hydrogen evolution, *Sep. Purif. Technol.*, 2025, **354**, 129089, DOI: **10.1016/j.seppur.2024.129089**.

19 Z. He, C. Qian, D. Chen, K. Xu and W. Hao, Design of ultrathin CoAl-LDHs/$ZnIn_2S_4$ with strong interfacial bonding and rich oxygen vacancies for highly efficient hydrogen evolution activity, *J. Colloid Interface Sci.*, 2023, **651**, 138–148, DOI: **10.1016/j.jcis.2023.07.179**.

20 L. Peng, *et al.*, Self-assembled transition metal chalcogenides@CoAl-LDH 2D/2D heterostructures with enhanced photoactivity for hydrogen evolution, *Inorg. Chem. Front.*, 2022, **9**(5), 994–1005, DOI: **10.1039/d1qi01603b**.

21 C. Tang, *et al.*, Bioinspired 3D penetrating structured micro-mesoporous NiCoFe-LDH@$ZnIn_2S_4$ Z-scheme heterojunction for simultaneously photocatalytic H_2 evolution coupled with benzylamine oxidation, *Appl. Catal., B*, 2024, **342**, 123384, DOI: **10.1016/j.apcatb.2023.123384**.

22 D. Wang, Z. Yang, Y. Xie, Y. Feng and J. Yao, NiCo Layered Double Hydroxide Bearing $ZnIn_2S_4$ Nanosheets for Highly Efficient Photocatalytic Cr(VI) Reduction, *ACS Appl. Nano Mater.*, 2023, **6**(7), 6086–6091, DOI: **10.1021/acsanm.3c00427**.

23 Q. Zhou, B. Jiang, L. Zhang, Y. Sun, X. Yang and L. Zhang, 1D/2D CoNi-LDH/$ZnIn_2S_4$ S-scheme heterojunction for effectively tetracycline degradation under photocatalytic-peroxymonosulfate activation system: DFT calculations and mechanism insights, *Chem. Eng. J.*, 2023, **478**, 147535, DOI: **10.1016/j.cej.2023.147535**.

24 Z. Jin, X. Wang, Y. Wang, T. Yan and X. Hao, Snowflake-like Cu_2S Coated with NiAl-LDH Forms a p-n Heterojunction for Efficient Photocatalytic Hydrogen Evolution, *ACS Appl. Energy Mater.*, 2021, **4**(12), 14220–14231, DOI: **10.1021/acsaem.1c02982**.

25 X. Lu, *et al.*, *2D Layered Double Hydroxide Nanosheets and Their Derivatives Toward Efficient Oxygen Evolution Reaction*, Springer Singapore, 2020, vol. 12. DOI: **10.1007/s40820-020-00421-5**.

26 S. Tonda, S. Kumar, M. Bhardwaj, P. Yadav and S. Ogale, G-C_3N_4/NiAl-LDH 2D/2D Hybrid Heterojunction for High-

Performance Photocatalytic Reduction of CO_2 into Renewable Fuels, *ACS Appl. Mater. Interfaces*, 2018, **10**(3), 2667–2678, DOI: **10.1021/acsami.7b18835**.

27 X. Deng, *et al.*, Carbon-Dots-Modified Hierarchical $ZnIn_2S_4$/Ni-Al LDH Heterojunction with Boosted Charge Transfer for Visible-Light-Driven Photocatalytic H_2 Evolution, *Inorg. Chem.*, 2023, **62**(24), 9702–9712, DOI: **10.1021/acs.inorgchem.3c01317**.

28 O. Cavdar, *et al.*, Photocatalytic hydrogen evolution from glycerol-water mixture under visible light over zinc indium sulfide ($ZnIn_2S_4$) nanosheets grown on bismuth oxychloride (BiOCl) microplates, *J. Colloid Interface Sci.*, 2023, **640**, 578–587, DOI: **10.1016/j.jcis.2023.02.129**.

29 C. Li, H. Li, L. Han, C. Li and S. Zhang, Ionothermal/hydrothermal synthesis of the ternary metal chalcogenide $ZnIn_2S_4$, *Mater. Lett.*, 2011, **65**(15–16), 2537–2540, DOI: **10.1016/j.matlet.2011.05.052**.

30 J. Chen, *et al.*, Nickel clusters accelerating hierarchical zinc indium sulfide nanoflowers for unprecedented visible-light hydrogen production, *J. Colloid Interface Sci.*, 2022, **608**, 504–512, DOI: **10.1016/j.jcis.2021.09.156**.

31 I. H. Choi, S. Y. Jang, H. C. Kim and S. Huh, In_6S_7 nanoparticle-embedded and sulfur and nitrogen co-doped microporous carbons derived from $In(tdc)_2$ metal-organic framework, *Dalton Trans.*, 2018, **47**(4), 1140–1150, DOI: **10.1039/c7dt03910g**.

32 M. Sigl, *et al.*, $ZnIn_2S_4$ thin films with hierarchical porosity for photocatalysis, *J. Mater. Chem. A*, 2024, **12**, 28965–28974, DOI: **10.1039/d4ta04237a**.

33 M. Yang, *et al.*, Atomic activation triggering selective photoreduction of CO_2 to CH_4 over NiAl-LDH/CeO_2 heterojunction, *Chem. Eng. J.*, 2023, **472**, 145071, DOI: **10.1016/j.cej.2023.145071**.

34 S. Megala, P. Ravi, P. Maadeswaran, M. Navaneethan, M. Sathish and R. Ramesh, The construction of a dual direct Z-scheme NiAl LDH/g-C_3N_4/Ag_3PO_4 nanocomposite for enhanced photocatalytic oxygen and hydrogen evolution, *Nanoscale Adv.*, 2021, **3**(7), 2075–2088, DOI: **10.1039/d0na01074j**.

35 X. Deng, *et al.*, Carbon-Dots-Modified Hierarchical $ZnIn_2S_4$/Ni–Al LDH Heterojunction with Boosted Charge Transfer for Visible-Light-Driven Photocatalytic H_2 Evolution, *Inorg. Chem.*, 2023, **62**(24), 9702–9712, DOI: **10.1021/acs.inorgchem.3c01317**.

36 S. Megala, *et al.*, Enhancement of photocatalytic H_2 evolution from water splitting by construction of two dimensional gC_3N_4/NiAl layered double hydroxides, *Appl. Surf. Sci.*, 2020, **509**, 144656, DOI: **10.1016/j.apsusc.2019.144656**.

37 W. K. Unger, J. C. Irwin and H. Pink, Printed in Great Britain RAMAN AND INFRARED SPECTRA OF $CdIn_2S_4$ and $ZnIn_2S_4$, *Solid State Commun.*, 1977, **25**, 913–915.

38 G. Good, *Angew. Chem., Int. Ed.*, 1967, **6**(11), 897–1011.

39 N. Baliarsingh, L. Mohapatra and K. Parida, Design and development of a visible light harvesting Ni-Zn/Cr-CO_3^{2-} LDH system for hydrogen evolution, *J. Mater. Chem. A*, 2013, **1**(13), 4236–4243, DOI: **10.1039/c2ta00933a**.

40 Y-F. Miao, *et al.*, Fabrication of β-In_2S_3/NiAl-LDH heterojunction photocatalyst with enhanced separation of charge carriers for efficient CO_2 photocatalytic reduction, *Appl. Surf. Sci.*, 2020, **527**, 146792, DOI: **10.1016/j.apsusc.2020.146792**.

41 Y. Wei, G. Cheng, J. Xiong, F. Xu and R. Chen, Positive Ni$(HCO_3)_2$ as a Novel Cocatalyst for Boosting the Photocatalytic Hydrogen Evolution Capability of Mesoporous TiO_2 Nanocrystals, *ACS Sustainable Chem. Eng.*, 2017, **5**(6), 5027–5038, DOI: **10.1021/acssuschemeng.7b00417**.

42 C. Rincke, S. Bette, R. E. Dinnebier and W. Voigt, Nickel Bicarbonate Revealed as a Basic Carbonate, *Eur. J. Inorg. Chem.*, 2015, **2015**(36), 5913–5920, DOI: **10.1002/ejic.201501094**.

43 Z. Da Gao, Y. F. Qu, X. Zhou, L. Wang, Y. Y. Song and P. Schmuki, Pt-Decorated g-C_3N_4/TiO_2 Nanotube Arrays with Enhanced Visible-Light Photocatalytic Activity for H2 Evolution, *ChemistryOpen*, 2016, **5**(3), 197–200, DOI: **10.1002/open.201500219**.

44 M. Zare, A. Mortezaali and A. Shafiekhani, Photoelectrochemical determination of shallow and deep trap states of platinum-decorated TiO_2 nanotube arrays for photocatalytic applications, *J. Phys. Chem. C*, 2016, **120**(17), 9017–9027, DOI: **10.1021/acs.jpcc.5b11987**.

45 J. Yu, K. Wang, W. Xiao and B. Cheng, Photocatalytic reduction of CO_2 into hydrocarbon solar fuels over g-C_3N_4-Pt nanocomposite photocatalysts, *Phys. Chem. Chem. Phys.*, 2014, **16**(23), 11492–11501, DOI: **10.1039/c4cp00133h**.

46 L. Wang, B. Cheng, L. Zhang and J. Yu, In situ Irradiated XPS Investigation on S-Scheme TiO_2@$ZnIn_2S_4$ Photocatalyst for Efficient Photocatalytic CO_2 Reduction, *Small*, 2021, **17**(41), 1–9, DOI: **10.1002/smll.202103447**.

47 S. Mao, *et al.*, Au nanodots@thiol-UiO66@$ZnIn_2S_4$ nanosheets with significantly enhanced visible-light photocatalytic H_2 evolution: The effect of different Au positions on the transfer of electron-hole pairs, *Appl. Catal., B*, 2021, **282**, 119550, DOI: **10.1016/j.apcatb.2020.119550**.

48 K. Wang, *et al.*, Z-Scheme Core-Shellmeso-TiO_2@$ZnIn_2S_4$/Ti_3C_2MXene Enhances Visible Light-Driven CO_2-to-CH_4 Selectivity, *Ind. Eng. Chem. Res.*, 2021, **60**(24), 8720–8732, DOI: **10.1021/acs.iecr.1c00713**.

49 W. K. Jo, S. Moru and S. Tonda, A green approach to the fabrication of a TiO_2/NiAl-LDH core-shell hybrid photocatalyst for efficient and selective solar-powered reduction of CO2 into value-added fuels, *J. Mater. Chem. A*, 2020, **8**(16), 8020–8032, DOI: **10.1039/d0ta00104j**.

50 J. S. Hammond and N. Winograd, XPS spectroscopic study of potentiostatic and galvanostatic oxidation of Pt electrodes in H_2SO_4 and $HClO_4$, *J. Electroanal. Chem. Interfacial Electrochem.*, 1977, **78**, 55–69.

51 A. Moulder and J. F. Chastain, *Handbook of X-ray Photoelectron Spectroscopy: A Reference Book of Standard Spectra for Identification and Interpretation of XPS Data*, Physical Electronics Division, Perkin-Elmer Corporation, 1992.

52 W. K. Chong, B. J. Ng, L. L. Tan and S. P. Chai, Recent Advances in Nanoscale Engineering of Ternary Metal

Sulfide-Based Heterostructures for Photocatalytic Water Splitting Applications, *Energy Fuels*, 2022, **36**(8), 4250–4267, DOI: **10.1021/acs.energyfuels.2c00291**.

53 R. Janani, R. Preethi, S. Singh, A. Rani and C. T. Chang, Hierarchical ternary sulfides as effective photocatalyst for hydrogen generation through water splitting: A review on the performance of znin2s4, *Catalysts*, 2021, **11**(2), 1–19, DOI: **10.3390/catal11020277**.

54 H. B. Michaelson, The work function of the elements and its periodicity, *J. Appl. Phys.*, 1977, **48**(11), 4729–4733, DOI: **10.1063/1.323539**.

55 N. Xiao, S. Li, X. Li, L. Ge, Y. Gao and N. Li, The roles and mechanism of cocatalysts in photocatalytic water splitting to produce hydrogen, *Chin. J. Catal.*, 2020, **41**(4), 642–671, DOI: **10.1016/S1872-2067(19)63469-8**.

56 X. Wang, *et al.*, Induced dipole moments in amorphous ZnCdS catalysts facilitate photocatalytic H_2 evolution, *Nat. Commun.*, 2024, **15**(1), 2600, DOI: **10.1038/s41467-024-47022-z**.

57 M. Wang, Y. Na, M. Gorlov and L. Sun, Light-driven hydrogen production catalysed by transition metal complexes in homogeneous systems, *Dalton Trans.*, 2009, 6458–6467, DOI: **10.1039/b903809d**.